Posted: August 19, 2023

Long-term hydrometeorological time-series analysis over the central highlands of West Papua

Sandy Hardian Susanto Herho[1, 2, *], Dasapta Erwin Irawan[3], Rubiyanto Kapid[4], and Siti Nurzannah Kaban[5]

[1]Department of Earth and Planetary Sciences, University of California, Riverside, USA
[2]Department of Geology, University of Maryland, College Park, USA
[3]Applied Geology Research Group, Bandung Institute of Technology (ITB), Bandung, Indonesia
[4]Geology Research Group, Bandung Institute of Technology (ITB), Bandung, Indonesia
[5]School of Architecture, Planning and Persevation, University of Maryland, College Park, USA
[*]Corresponding author: sandy.herho@email.ucr.edu

Abstract

The article introduces an innovative data-driven approach to examining the long-term temporal rainfall patterns in the central highlands of West Papua, Indonesia. Through the utilization of wavelet transforms, we identified signs of a negative temporal correlation between the El Niño-Southern Oscillation (ENSO) and the 12-month Standardized Precipitation Index (SPI-12).

Building upon this cause-and-effect relationship, we employed dynamic causality modeling, utilizing the Nonlinear Autoregressive with Exogenous input (NARX) model, to predict SPI-12. In this predictive framework, the Multivariate ENSO Index (MEI) was employed as an attribute variable. Consequently, this dynamic neural network model effectively captured common patterns within the SPI-12 time series.

The implications of this study extend significantly to the advancement of data-driven precipitation models for regions characterized by intricate topography within the Indonesian Maritime Continent (IMC).

1 Introduction

The central highlands of West Papua form an integral part of the province of Papua, situated as the easternmost province of Indonesia (Figure 1). This region boasts a complex landscape, characterized by rugged and hilly terrain. Notably, some of Indonesia's highest peaks, including Carstensz Pyramid (5030 m.a.s.l.), Trikora Peak (4730 m.a.s.l.), Yamin Peak (4595 m.a.s.l.), and Mandala Peak (4700 m.a.s.l), are nestled within the central highlands of West Papua. The intricate geomorphological features of this area serve as a manifestation of the geological and tectonic processes that have shaped its topography.

According to Pigram and Symonds (1991), the formation of the Papua island emerged from the subduction process between the Australian Plate and the Pacific Plate. This convergent process and the resultant deformation of these plates commenced in the Eocene era and have persisted up to the present day (Charlton, 2000). The Australian Plate, lying beneath the Arafura Sea and extending northward, forms the foundation of the southern segment of the central highlands of West Papua. This foundation comprises sedimentary rocks of various ages, ranging from Paleozoic to Mid-Quaternary (Dow and Sukamto, 1984).

Stretching from the equator to 12°S, the central highlands of West Papua qualify as a tropical region largely influenced by the monsoonal asymmetric cycle, akin to the prevailing conditions across much of the Indonesian Maritime Continent (IMC) (Ramage, 1968; Neale and Slingo, 2003; Chang et al., 2005; Yang et al., 2019). In tandem with these monsoonal influences, the area is subject to localized effects, including mountain deflection and local warming, which exert control over rainfall patterns (Boerema, 1938). Additionally, the El Niño-Southern Oscillation (ENSO) phenomenon leaves its imprint on the seasonal rainfall dynamics in Papua; El Niño events, for instance, can lead to reduced rainfall in the region (Permana et al., 2016).

The central highlands of West Papua experience varying precipitation levels spanning from 2500 to 4500 mm/year. The number of rainy days varies from 148 to 175 per year, while average surface air temperatures fluctuate between 29°C and 31.8°C. Relative humidity in the area ranges between 79% and 81%. Consequently, the central highlands of Papua emerges as one of the most moisture-laden regions within the IMC (Marshall and Beehler, 2007).

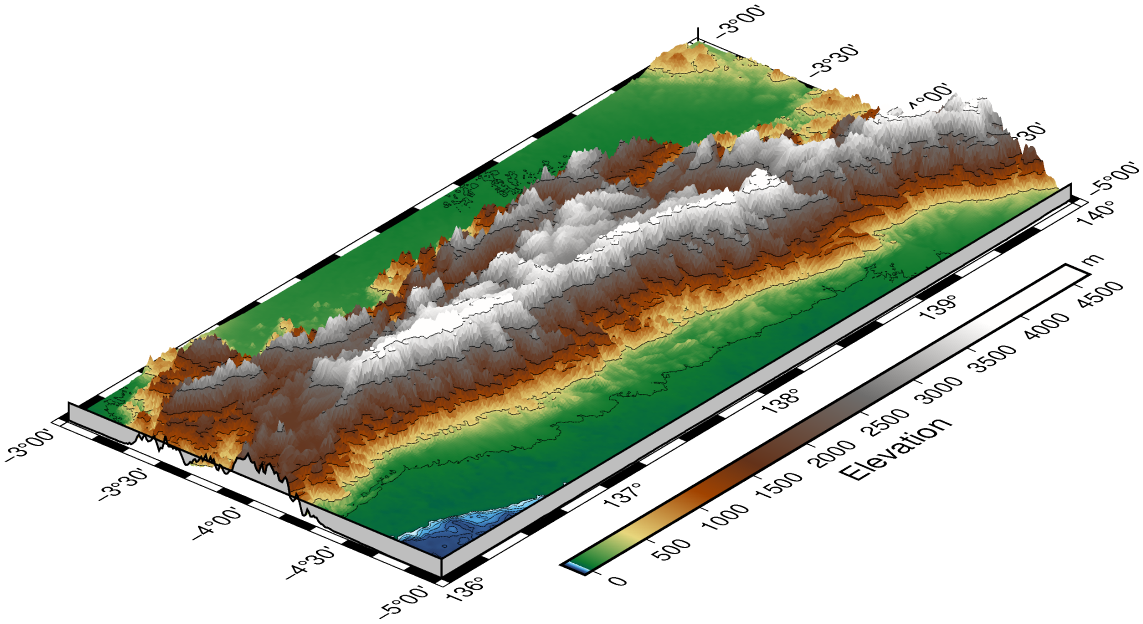

Figure 1: Digital Elevation Model (DEM) of the central highlands of West Papua (rendered using **PyGMT** (Wessel et al., 2019)).

Studies delving into the rainfall characteristics of the Papua region remain scarce, posing a challenge for researchers to access pertinent information. This scarcity might stem from the intricate topography prevalent in this area, rendering conventional numerical approaches challenging for investigation (e. g. Goger et al., 2016; Chow et al., 2019; Largeron et al., 2020; Clifton et al., 2022). Furthermore, the limitations imposed by the aerial distribution of rain gauges and radar networks, under the purview of the Indonesian Agency for Meteorology, Climatology and Geophysics (BMKG), could also contribute to this dearth (Yamanaka, 2016).

To address this issue, we propose a solution that employs a data-driven approach (Peters-Lidard et al., 2017). By leveraging ERA5 monthly averaged data at single levels (Hersbach et al., 2020), we aim to uncover the attributes and predictability of long-term precipitation time series across the central highlands of Papua. This approach offers an alternative means to examine and understand the nuanced aspects of rainfall behavior in the region, circumventing the challenges posed by complex terrain and sparse meteorological instrumentation.

2 Materials and Methods

2.1 Long-term drought / pluvial time-series reconstruction

In this subsection, our focus lies in reconstructing long-term meteorological drought and pluvial events within the central highlands of West Papua. To quantitatively assess these occurrences, we employed the SPI-12 index (McKee et al., 1993; Guttman, 1999), a well-established metric for evaluating extended meteorological droughts and pluvial periods. This index's effectiveness in reconstructing droughts spanning the past millennium within the Indonesian Maritime Continent (IMC) has been documented (Herho et al., 2018).

Our initial step entailed computing the spatial average of terrestrial precipitation across the central highlands of West Papua, utilizing the ERA5 monthly averaged data on single levels (Hersbach et al., 2020). Mathematically defined in equation 1, the spatial average for a precipitation field $\overline{p}(\phi, \theta, t)$ on a spherical surface (Shen and Somerville, 2019) is expressed as:

$$\overline{p}(t) = \frac{1}{4\pi}\int\int p(\phi,\theta,t)\cos(\phi)d\phi d\theta \tag{1}$$

, where ϕ is latitude, θ is longitude, and t is time. To handle the gridded dataset, a discretized form of equation (1) was needed.The discrete form of equation (1) for a grid resolution $\Delta\phi \times \Delta\theta$ is defined in equation (2):

$$\overline{p}(t) = \sum_{i,j} p(i,j,t)\frac{\cos(\phi_{i,j})\Delta\phi\Delta\theta}{4\pi} \tag{2}$$

, where (i,j) are coordinate indices for each the grid box of precipitation data over the central highlands of West Papua, and ϕ and θ are in radian. Since ERA5 precipitation data has a spatial resolution of $0.25° \times 0.25°$, then $\Delta\phi = \Delta\theta = (0.25/180)\pi = \pi/720$. By substituting this information into equation (2), the following equation was obtained:

$$\overline{p}(t) = \sum_{i,j} p(i,j,t)\frac{\cos(\phi_{i,j})(1/720)^2}{4} \tag{3}$$

We solved the calculation in the equation (3) using the built-in function in the **xarray** library (Hoyer and Hamman, 2017) in the Python computational environment.

The spatial average of monthly precipitation was subsequently employed as input for calculating SPI-12. SPI-12 itself entailed the comparison of the rainfall over 12 consecutive months with the corresponding 12 months from preceding years. The SPI at this temporal scale provided insights into long-term rainfall patterns (McKee et al., 1993; Guttman, 1999). This time scale represented the cumulative effect of prior periods that could have been either above or below the normal range. SPI at this scale could be correlated with streamflows, reservoir conditions, and even groundwater levels. In several countries, SPI-12 exhibited the closest correlation with the Palmer Drought Severity Index (PDSI), and it was conceivable that both indices reflected the same conditions (Guenang and Kamga, 2014).

SPI was calculated using statistical methods as follows:

$$G(x) = \int_0^x g(x,\hat{\alpha},\hat{\beta})dx = \frac{1}{\hat{\beta}^{\hat{\alpha}}\Gamma(\hat{\alpha})}\int_0^x x^{\hat{\alpha}-1}e^{-x/\hat{\beta}} \tag{4}$$

, where α is a shape parameter, β is a scale parameter, $\Gamma(\alpha)$ is a gamma function, and x is precipitation values. Equation (4) applies if $x > 0$ (otherwise $g(x,\hat{\alpha},\hat{\beta}) = 0$, which in this case applied to precipitation data which are always within the range $(0,+\infty)$. In order to match the gamma distribution with precipitation data, it was necessary to estimate the α and β parameters using the maximum likelihood approximation which is defined as follows:

$$\hat{\alpha} = \frac{1}{4A}\left(1 + \sqrt{\frac{4A}{3}}\right) \tag{5}$$

$$\hat{\beta} = \frac{\overline{x}}{\hat{\alpha}} \tag{6}$$

, where A is defined by equation (7),

$$A = \ln(\overline{x}) - \frac{\sum\ln(x)}{n} \tag{7}$$

, where n is the number of observations. For $\hat{\alpha} > 0$, $\Gamma(\hat{\alpha})$ is defined by equation (8),

$$\Gamma(\hat{\alpha}) = \int_0^{+\infty} x^{(\hat{\alpha}-1)}e^{-x}dx \tag{8}$$

The gamma distribution is undefined for $x = 0$ and $q = P(x = 0) > 0$, where q is the probability of zero percipitation. Therefore the cumulative probability distribution is defined by equation (9):

$$H(x) = q + (1-q)G(x) \tag{9}$$

The gamma distribution $G(x)$ was then converted to be a normal standard with zero mean and standard deviation of one, so that the SPI index Z was obtained using equation (10):

$$Z = \begin{cases} -t - \frac{c_0+c_1t+c_2t^2}{1+d_1t+d_2t^2+d_3t^3}, & \text{for } 0 < H(x) \leq 0.5 \\ t - \frac{c_0+c_1t+c_2t^2}{1+d_1t+d_2t^2+d_3t^3}, & \text{for } 0.5 < H(x) < 1 \end{cases} \tag{10}$$

, where t is defined by equation (11):

$$t = \begin{cases} \sqrt{\ln\left(\frac{1}{(H(x))^2}\right)}, & \text{for } 0 < H(x) \leq 0.5 \\ \sqrt{\ln\left(\frac{1}{(1-H(x))^2}\right)}, & \text{for } 0.5 < H(x) < 1 \end{cases} \tag{11}$$

, and the constants are defined as follows:

$$\begin{cases} c_0 = 2.516, \\ c_1 = 0.803, \\ c_2 = 0.01, \\ d_1 = 1.433, \\ d_2 = 0.109, \\ d_3 = 0.001 \end{cases} \tag{12}$$

In order to simplify the calculation process, we used the **SPEI** package (Beguería and Vicente-Serrano, 2017) in the R computational environment.

2.2 Identifying ENSO-driven pattern in SPI-12

The influence of the ENSO signal within the IMC (Permana et al., 2016; Yamanaka, 2016; Yoden et al., 2017) constitutes an undeniable aspect that demands thorough consideration within the analysis of drought and pluvial events in the central highlands of West Papua. This subsection comprehensively examines the temporal ramifications of ENSO, employing the Multivariate ENSO Index (MEI) (Wolter and Timlin, 2011), with regard to SPI-12. In order to gauge the temporal repercussions of ENSO on drought and pluvial occurrences across the designated study area, we utilized the prevalent algorithm for scrutinizing geophysical signal patterns—namely, wavelet transforms. The inherent advantage of wavelet transforms over alternative power spectrum methods lies in their aptitude for capturing non-linear signals within time series data, achieved through the utilization of discrete wave packets (wavelets) characterized by inherently smooth terminations, as opposed to the conventional employment of sine and cosine wave functions (Lau and Weng, 1995).

In this study we used an extension of the Morlet wavelet (ψ) (Torrence and Compo, 1998) to model ENSO and SPI-12 signals, which is defined by:

$$\psi(t) = \pi^{-\frac{1}{4}} e^{-i\omega_0 t} e^{-\frac{1}{2}t^2}, t = 1, 2, 3, \cdots \tag{13}$$

, where t is the position where the wavelet operates in a time series with a narrow range of observations.

In general, wavelets have two main components, namely time or position k and frequency f. The k parameter has an important role in detecting the exact location of a wavelet by relocating the wavelet over a period of time, while f is useful for monitoring the convex wavelet to localize different frequencies. By transforming ψ, we got the $\psi_{k,f}$ parameter as follows:

$$\psi_{k,f}(t) = \frac{1}{\sqrt{h}} \psi\left(\frac{t-k}{f}\right), \; k, f \in R, \; f \neq 0 \tag{14}$$

Equation (15) describes the modeling of a time series $x(t)$ into a wavelet transform,

$$W_x(k, f) = \int_{-\infty}^{+\infty} x(t) \frac{1}{\sqrt{f}} \psi\left(\overline{\frac{(t-k)}{f}}\right) dt \tag{15}$$

The signal power in the time series $x(t)$ itself was measured using the wavelet power spectrum $\text{WPS}_x(k, f)$ which is defined as follows:

$$\text{WPS}_x(k, f) = |W_x(k, f)|^2 \tag{16}$$

In order to simplify the process of calculating the continuous wavelet power spectrum on ENSO and SPI-12 data, we used the **PyCWT** library (Krieger et al., 2017) in the Python computational environment.

To measure the relationship between the two quantitatively, we needed another mathematical tool, namely the wavelet coherence (WTC). We used WTC to find time-frequency-based causality between two time-series data, in this context MEI. $x(t)$ and SPI-12 $y(t)$. The first step we take was to find the cross wavelet transform (XWT) of the two time-series data (equation (17)):

$$W_{xy}(k, f) = W_x(k, f)\overline{W_y(k, f)} \tag{17}$$

, where $W_{x,y}(k, f)$ is the XWT of the two time-series data. Then to find WTC value, the equation (18) was used as follows,

$$R^2(k, f) = \frac{|C\left(f^{-1}W_{xy}(k, f)\right)|^2}{C\left(f^{-1}|W_x(k, f)|^2\right)C\left(f^{-1}|W_y(k, f)|^2\right)} \tag{18}$$

, C parameter shows the time and smoothing process over the duration of time in within the range of $0 \leq R^2(k, f) \leq 1$. When $R^2(k, f)$ approaches one, a strong correlation can be expected between MEI and SPI-12. Conversely, if $R^2(k, f)$ is zero, then there is no correlation between the two variables. To find out the positive or negative correlation of the two time-series data, we use the phase difference equation (equation (19)) as follows:

$$\phi_{xy}(k, f) = \arctan\left(\frac{\Im\left\{C\left(f^{-1}W_{xy}(k, f)\right)\right\}}{\Re\left\{C\left(f^{-1}W_{xy}(k, f)\right)\right\}}\right) \tag{19}$$

, where $\Re$ shows the real part and $\Im$ shows the imaginary part. To simplify the WTC calculation process, we used the open source MATLAB® Toolbox by Grinsted et al. (2004).

2.3 ENSO - SPI-12 dynamic relationship and predictability

To ensure the production of accurate SPI-12 predictions, we employed the Nonlinear Autoregressive with Exogenous input neural networks (NARX) model. This model was adept at capturing the dynamic relationship between ENSO and long-term drought/pluvial events across the central highlands of West Papua. NARX, characterized as a type of recurrent dynamic neural network, was extensively employed to model the non-linear associations within attributes across time series data (Diaconescu, 2008; Ang et al., 2014; Caswell, 2014). A schematic representation of the simplified NARX structure is provided in Figure 2. Input data was introduced into delay units, which functioned as memory repositories for previous inputs. Outputs derived from the NARX model were also stored within delay units, subsequently directed into hidden units for further processing.

NARX model is defined as a nonlinear mapping function f (Diaconescu, 2008) as follows:

$$y_t = f\left(y_{t-1}, y_{t-2}, \cdots, y_{t-d_y}, x_{t-1}, x_{t-2}, \cdots x_{t-d_x}\right) \tag{20}$$

, where y is a target (SPI-12) and x are attributes (MEI); and $d_x \geq 1$, $d_y \geq 1$, $d_y \geq d_x$ are delays. The nonlinear f function itself is generally unknown, and must be approximated using the existing data. There are various ways to approximate this function, in this study we use multilayer perceptrons provided by **PyNeurGen** library (Smiley, 2012) in the Python computational environment. We used 1 time steps of delay for each of the input (x) and output (y) attributes. In addition, we also split incoming weights, 60% for MEI and 30% for SPI-12. We made use of the following sigmoid function for activation of the perceptrons:

$$S(x) = \frac{1}{1 + e^{-x}} \tag{21}$$

We divided SPI-12 into two parts, 85% for the training set and 15% (January 1980 - December 2014) for the testing set (January 2015 - December 2020). We used a moderate steps of learning rate of 35% for the optimization process using the Stochastic Gradient Descent (SGD) algorithm. Our NARX model was run for 10 epochs without activating the random testing parameter to maintain the order of time-series data. To

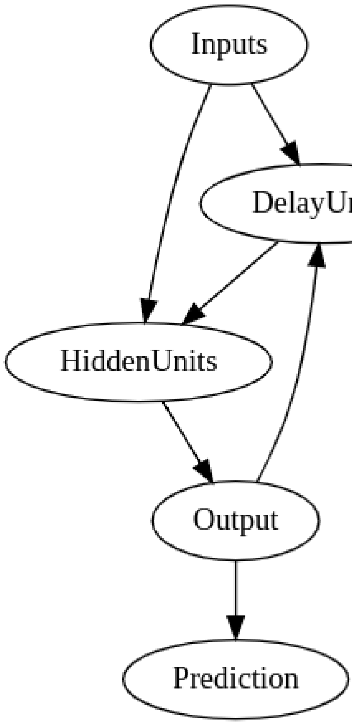

Figure 2: Simple schematic diagram of NARX model.

evaluate the model performance, we used the Mean Squared Error (MSE) which is shown by equation (22) below:

$$MSE = \frac{1}{n}\sum_{i=1}^{n}(\hat{y}_i - y_i)^2 \tag{22}$$

, which is the sum series of the squared differences of the observed target y_i and predicted values $\hat{y}_i$, which was then divided by the total number of test samples n.

3 Results and Discussion

The calculation result of equation (3) is the spatial average of monthly precipitation time-series shown in Figure 3. Figure 3 shows that rainfall events occurred in each month in this period of study. To see the pattern of monthly rainfall, we average the data for each month, as shown in Figure 4. It can be seen in Figure 4 that the monthly rainfall pattern in the central highlands of West Papua has one peak and one trough, which corresponds to the rainfall pattern in Region A (Aldrian and Susanto, 2003) with a shift in the onset of wet and dry seasons which is thought to be caused by other local factors. The seasonal rainfall patterns over the central highlands of West Papua (Figure 4) seem to follow an asymmetric pattern between boreal summer and winter and between boreal spring and fall.

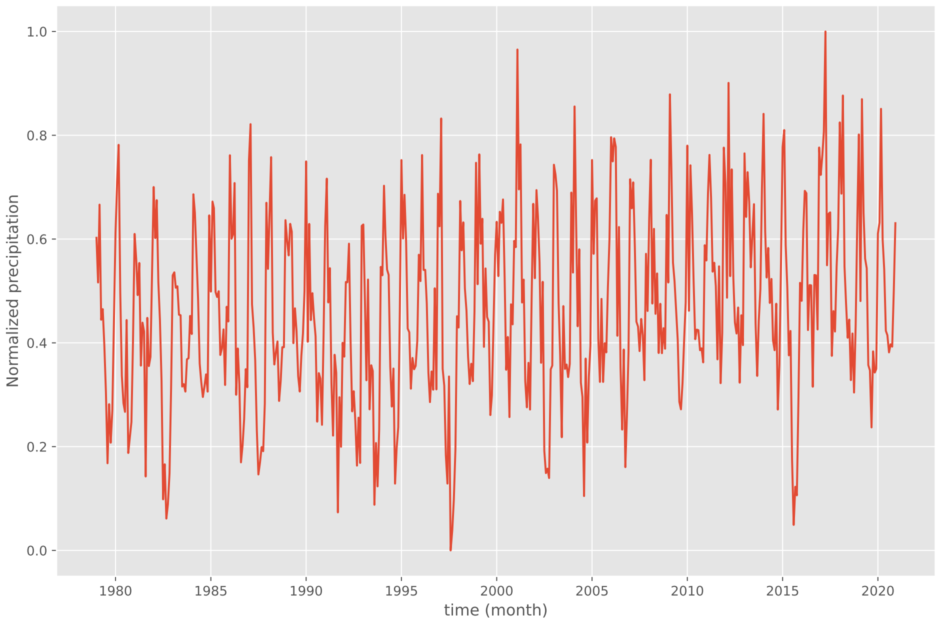

Figure 3: Variations in the normalized monthly precipitation data from ERA5 over the central highlands of West Papua from January 1979 to December 2020.

The result of the SPI-12 reconstruction for the period January 1980 to December 2020 is shown in Figure 5. There are similarities of WPS between ENSO (Figure 6) and SPI-12 (Figure 7). In order to ascertain the relationship between SPI-12 and MEI with greater quantitative rigor, a meticulous WTC computation was undertaken. The outcomes of this WTC calculation are elegantly presented in Figure 8, furnishing a graphical illustration that effectively encapsulates the derived results.

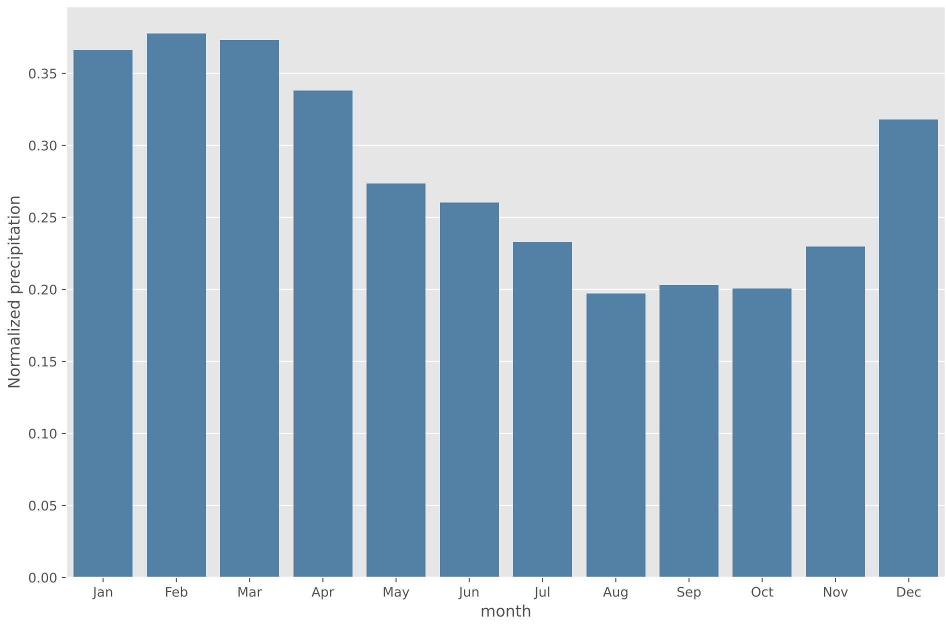

Figure 4: Normalized average monthly precipitation over the central highlands of Papua.

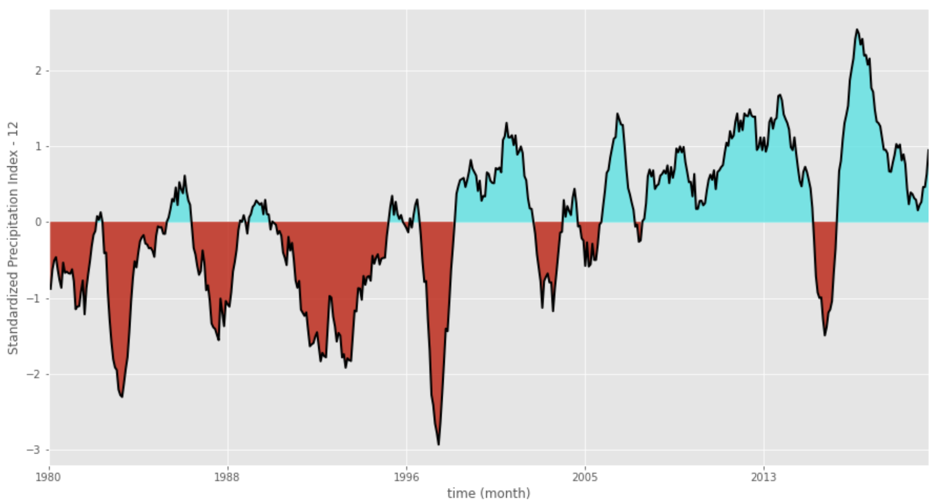

Figure 5: SPI values over the central highlands of West Papua from January 1980 to December 2020 with a 12-month time scale. Negative SPI-12 describes dry conditions (red), whereas positive SPI-12 describes wet conditions (blue).

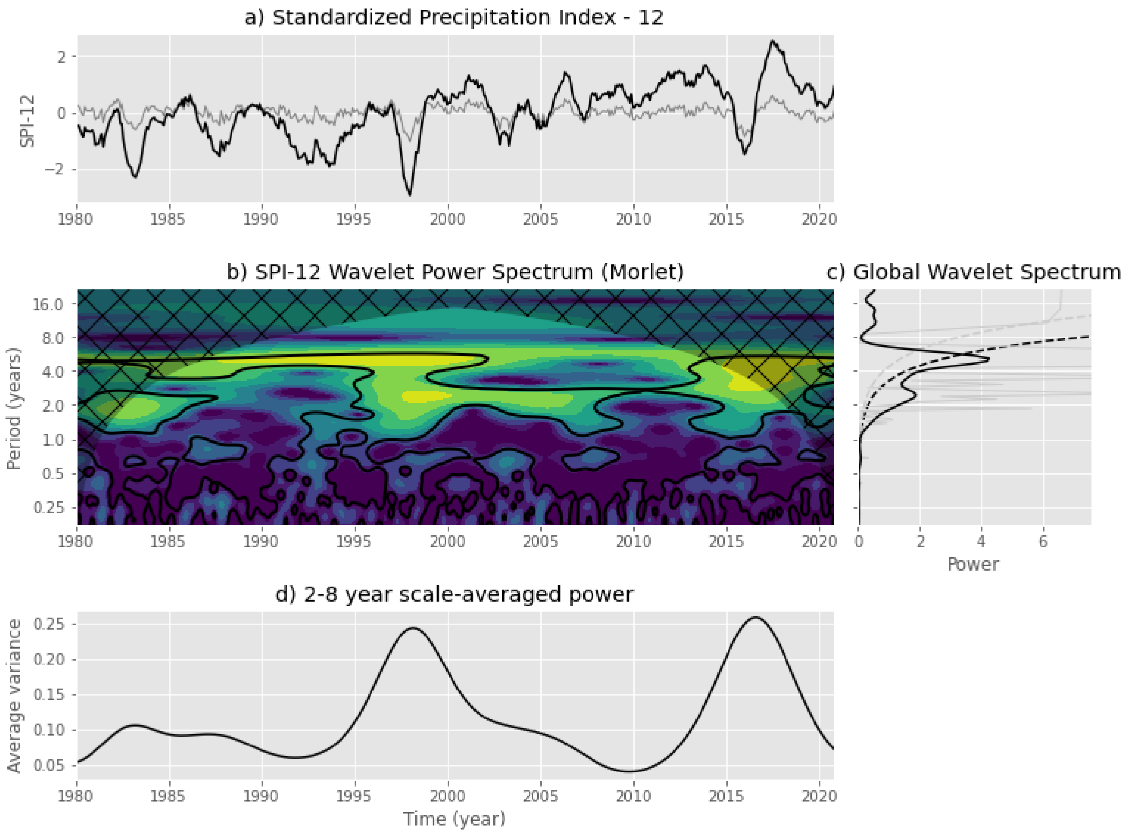

Figure 6: Continuous wavelet transform for the SPI-12. These plots clearly shows significant periodicity at 2 - 8 year cycle.

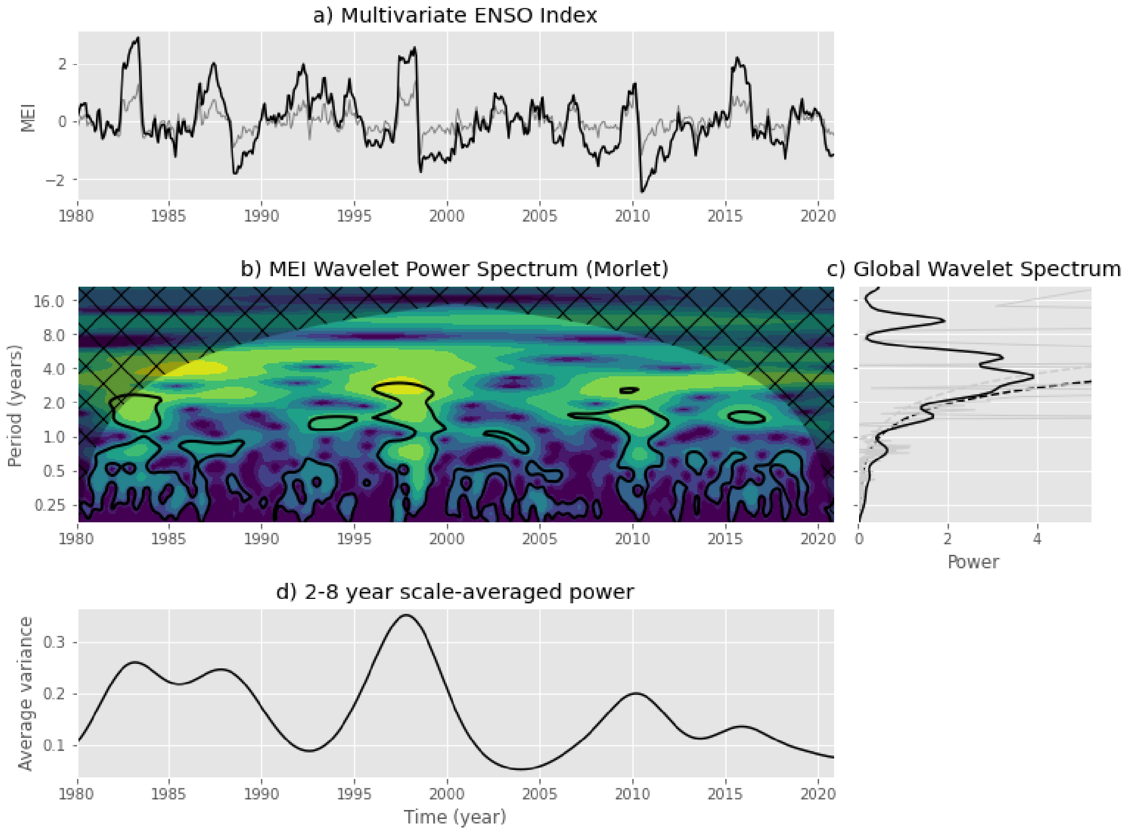

Figure 7: Continuous wavelet transform for the MEI. These plots clearly shows significant periodicity at 2 - 8 year cycle.

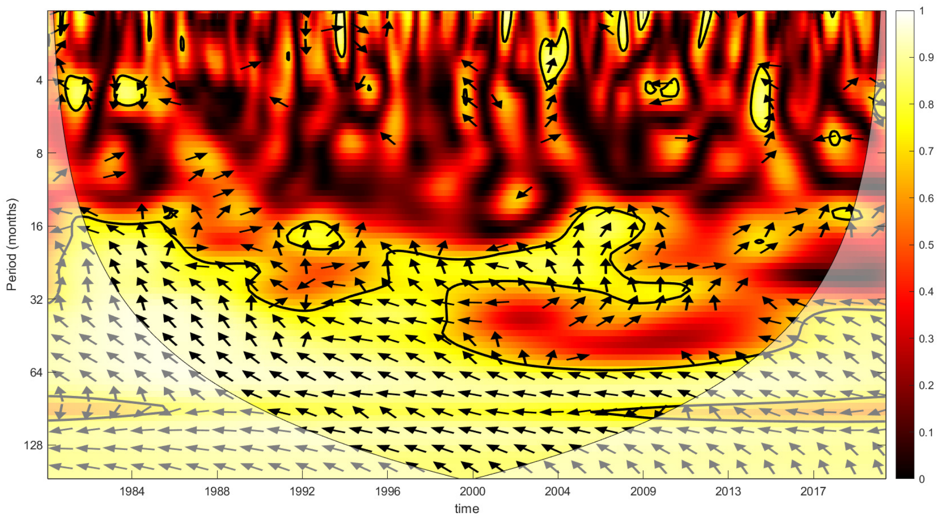

Figure 8: Wavelet coherence between MEI and SPI-12. The color scale on the right side of the figure represents the level of correlation between ENSO and long-term meteorological drought/pluvial events over the central highlands of West Papua. The light yellow color indicates high correlations among the variables, while the thick black contour designates the 5% significance level against red noise and the cone of influence (COI) where edge effects might distort the picture is shown as a lighter shade. The arrows show the phasing direction (**right**: in-phase, **left**: anti-phase, **down**: MEI leading SPI-12 by $\pi/2$, **up**: SPI-12 leading MEI by $\pi/2$).

As seen in Figure 8, WTC can capture the inversely proportional relationship between MEI and SPI-12 at 32 to 128 month periodicity. This causal effect reveals that precipitation over the central highlands of West Papua increases during La Niña and decreases during El Niño.

The MSE of NARX model at each training epoch can be seen in Figure 9. It exhibits sharp decline at the first epoch and finally leveling out until the end of the last training epoch. The overall MSE evaluation result in the test set is 0.011. The comparison between the NARX model prediction results and the actual SPI-12 is shown in Figure 10. Overall, the model tends to overestimate and underestimate certain extreme values, although it adequately captures the general pattern of SPI-12.

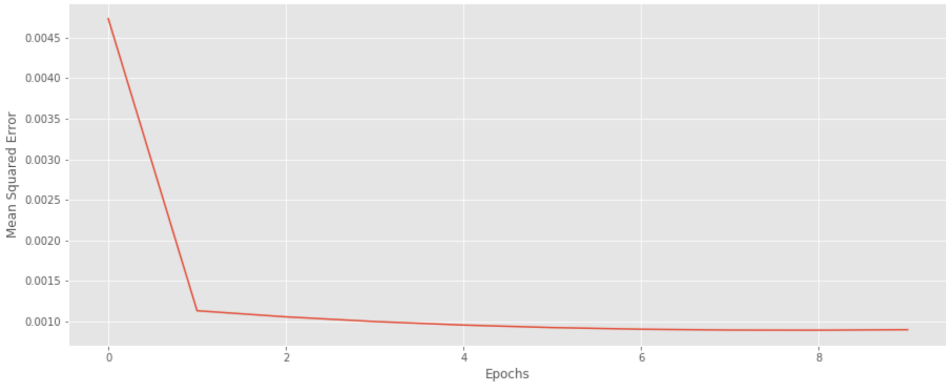

Figure 9: MSE by epoch for NARX model.

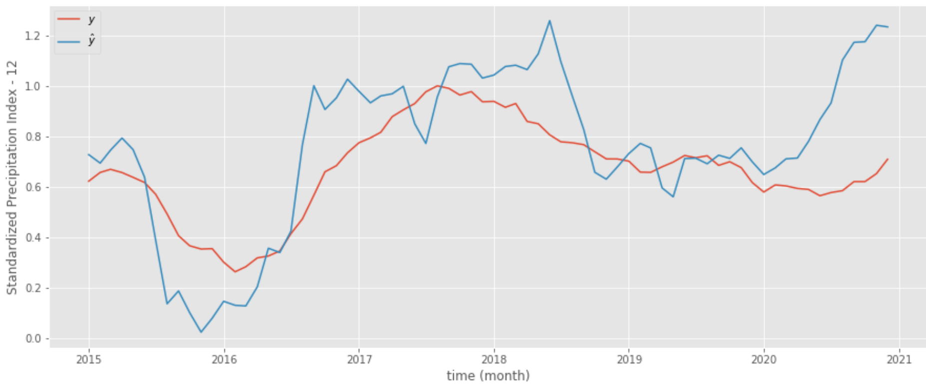

Figure 10: Actual y (red) and predicted $\hat{y}$ (blue) SPI-12 values for NARX model.

4 Conclusion

Our research endeavors encompassed an in-depth analysis of the SPI-12 time series dataset spanning the central highlands of West Papua. Through a rigorous exploration, we aimed to unravel the intricate relationships within this dataset, specifically focusing on the teleconnection pattern that exists between ENSO and hydrometeorological drought/pluvial events in this particular geographical region. Employing the potent methodology of wavelet transformations, we embarked on a meticulous journey to decipher the underlying connections.

Our meticulous investigation has led us to unveil a discernible and noteworthy teleconnection pattern between ENSO and hydrometeorological drought/pluvial events in the central highlands of West Papua. The complex web of relationships between these factors was elucidated through the prism of wavelet transformations, revealing a finely woven tapestry of associations. The outcome of our analysis pointed towards a significant and negative correlation between ENSO and the prevailing long-term rainfall patterns in this region. This finding is a crucial piece in the puzzle of understanding the dynamics of climatic events in this area.

Capitalizing on the patterns discerned from the wavelet coherence (WTC) analysis, we proceeded to construct a model that could encapsulate the nuanced temporal dynamics between ENSO and the intricate long-term rainfall patterns. This endeavor was facilitated through the strategic implementation of the NARX algorithm. The NARX model, renowned for its efficacy in capturing complex non-linear relationships, served as the tool through which we could delve deeper into the interplay of climatic variables.

The predictions gleaned from the NARX model bore testimony to its effectiveness in capturing the overarching trends embedded within the complex interdependence of ENSO and long-term rainfall patterns. The model's ability to encapsulate these trends augments our understanding of the underlying dynamics that govern these climatic phenomena. By distilling intricate data patterns into comprehensible insights, the NARX model emerges as a valuable asset in unraveling the complex tapestry of climatic interactions.

In light of our study's findings, there emerges a realm of potential avenues for further exploration and refinement. One avenue involves the application of diverse, finely-tuned optimization strategies to the NARX model, drawing inspiration from the work of He et al. (2021). Moreover, we recognize the significance of implementing early-stopping algorithms, as advocated by Gençay and Qi (2001), to safeguard against the perils of overfitting during model training.

Beyond the NARX model, a compelling need arises to conduct a comprehensive comparison involving a spectrum of robust sequence-to-sequence (seq2seq) machine learning algorithms. These include the Long-Short Term Memory (LSTM) (Hochreiter and Schmidhuber, 1997), the Gated Recurrent Unit (GRU) (Gers et al., 1999), and the DeepAR model (Salinas et al., 2020). This comprehensive evaluation aims to ascertain the optimal time-series model that faithfully encapsulates the intricate interplay of climatic variables in our dataset.

Furthermore, our study underscores the importance of juxtaposing our findings with the outputs derived from Global Climate Models (GCMs). This comparative analysis can potentially illuminate the intricate physical processes underpinning the spatio-temporal dynamics connecting ENSO and long-term rainfall patterns across the central highlands of West Papua. In doing so, we can achieve a more holistic comprehension of the complex interactions that govern the climatic landscape of this region.

References

Aldrian, E. and Susanto, R. D. (2003). Identification of three dominant rainfall regions within indonesia and their relationship to sea surface temperature. *International Journal of Climatology*, 23(12):1435–1452.

Ang, M. R. C. O., Gonzalez, R. M., and Castro, P. P. M. (2014). Multiple data fusion for rainfall estimation using a NARX-based recurrent neural network – the development of the REIINN model. *IOP Conference Series: Earth and Environmental Science*, 17:012019.

Beguería, S. and Vicente-Serrano, S. (2017). *SPEI: Calculation of the Standardised Precipitation-Evapotranspiration Index*. R package version 1.7.

Boerema, J. (1938). *Van Den Typen Regenval in Nederlandsch Indie (Rainfall types in Nederlands Indies)*. The Royal Observatory Magnetisch En Meteorologisch Batavia, Batavia.

Caswell, J. M. (2014). A nonlinear autoregressive approach to statistical prediction of disturbance storm time geomagnetic fluctuations using solar data. *Journal of Signal and Information Processing*, 5:42–53.

Chang, C.-P., Wang, Z., McBride, J., and Liu, C.-H. (2005). Annual Cycle of Southeast Asia—Maritime Continent Rainfall and the Asymmetric Monsoon Transition. *Journal of Climate*, 18(2):287 – 301.

Charlton, T. R. (2000). Tertiary evolution of the Eastern Indonesia Collision Complex. *Journal of Asian Earth Sciences*, 18(5):603–631.

Chow, F. K., Schär, C., Ban, N., Lundquist, K. A., Schlemmer, L., and Shi, X. (2019). Crossing multiple gray zones in the transition from mesoscale to microscale simulation over complex terrain. *Atmosphere*, 10(5):274.

Clifton, A., Barber, S., Stökl, A., Frank, H., and Karlsson, T. (2022). Research challenges and needs for the deployment of wind energy in hilly and mountainous regions. *Wind Energy Science*, 7(6):2231–2254.

Diaconescu, E. (2008). The use of narx neural networks to predict chaotic time series. *World Scientific and Engineering Academy and Society (WSEAS)*, 3(3):182–191.

Dow, D. B. and Sukamto, R. (1984). Western Irian Jaya: The end-product of oblique plate convergence in the late tertiary. *Tectonophysics*, 106(1):109–139.

Gençay, R. and Qi, M. (2001). Pricing and hedging derivative securities with neural networks: Bayesian regularization, early stopping, and bagging. *IEEE Transactions on Neural Networks*, 12:726 – 734.

Gers, F. A., Schmidhuber, J., and Cummins, F. (1999). Learning to forget: continual prediction with lstm. In *1999 Ninth International Conference on Artificial Neural Networks ICANN 99. (Conf. Publ. No. 470)*, volume 2, pages 850–855.

Goger, B., Rotach, M. W., Gohm, A., Stiperski, I., and Fuhrer, O. (2016). Current challenges for numerical weather prediction in complex terrain: Topography representation and parameterizations. In *2016 International Conference on High Performance Computing Simulation (HPCS)*, pages 890–894.

Grinsted, A., Moore, J. C., and Jevrejeva, S. (2004). Application of the cross wavelet transform and wavelet coherence to geophysical time series. *Nonlinear Processes in Geophysics*, 11(5/6):561–566.

Guenang, G. M. and Kamga, F. M. (2014). Computation of the standardized precipitation index (spi) and its use to assess drought occurrences in cameroon over recent decades. *Journal of Applied Meteorology and Climatology*, 53(10):2310 – 2324.

Guttman, N. B. (1999). Accepting the standardized precipitation index: A calculation algorithm1. *Journal of the American Water Resources Association*, 35(2):311–322.

He, X., Zhao, K., and Chu, X. (2021). Automl: A survey of the state-of-the-art. *Knowledge-Based Systems*, 212:106622.

Herho, S., Syahputra, M. R., and Suwarman, R. (2018). A preliminary study of meteorological drought influences to social events over the maritime continent during the last millennium. In *Extended Abstract 98th American Meteorological Society Annual Meeting*, 16th History Symposium, Austin, TX. American Meteorological Society.

Hersbach, H., Bell, B., Berrisford, P., Hirahara, S., Horányi, A., Muñoz-Sabater, J., Nicolas, J., Peubey, C., Radu, R., Schepers, D., Simmons, A., Soci, C., Abdalla, S., Abellan, X., Balsamo, G., Bechtold, P., Biavati, G., Bidlot, J., Bonavita, M., De Chiara, G., Dahlgren, P., Dee, D., Diamantakis, M., Dragani, R., Flemming, J., Forbes, R., Fuentes, M., Geer, A., Haimberger, L., Healy, S., Hogan, R., Hólm, E., Janisková, M., Keeley, S., Laloyaux, P., Lopez, P., Lupu, C., Radnoti, G., de Rosnay, P., Rozum, I., Vamborg, F., Villaume, S., and Thépaut, J. (2020). The ERA5 global reanalysis. *Quarterly Journal of the Royal Meteorological Society*, 146(730):1999–2049.

Hochreiter, S. and Schmidhuber, J. (1997). Long Short-Term Memory. *Neural Computation*, 9(8):1735–1780.

Hoyer, S. and Hamman, J. (2017). xarray: N-D labeled arrays and datasets in Python. *Journal of Open Research Software*, 5(1).

Krieger, S., Freij, N., Brazhe, A., Torrence, C., and Compo, G. P. (2017). *PyCWT: spectral analysis using wavelets in Python*. Python library version 0.3.0a22.

Largeron, C., Dumont, M., Morin, S., Boone, A., Lafaysse, M., Metref, S., Cosme, E., Jonas, T., Winstral, A., and Margulis, S. A. (2020). Toward snow cover estimation in mountainous areas using modern data assimilation methods: A review. *Frontiers in Earth Science*, 8:325.

Lau, K.-M. and Weng, H. (1995). Climate signal detection using wavelet transform: How to make a time series sing. *Bulletin of the American Meteorological Society*, 76(12):2391 – 2402.

Marshall, A. and Beehler, B. M. (2007). *The Ecology of Papua*, volume 1. Periplus Editions (HK), Singapore.

McKee, T. B., Doesken, N. J., and Kleist, J. (1993). The relationship of drought frequency and duration of the time scales. In *Proceeding 8th Conference on Applied Climatology*, Anaheim, CA. American Meteorological Society.

Neale, R. and Slingo, J. (2003). The Maritime Continent and its role in the global climate: A GCM study. *Journal of Climate*, 16(5):834–848.

Permana, D. S., Thompson, L. G., and Setyadi, G. (2016). Tropical West Pacific moisture dynamics and climate controls on rainfall isotopic ratios in southern Papua, Indonesia. *Journal of Geophysical Research: Atmospheres*, 121(5):2222–2245.

Peters-Lidard, C. D., Clark, M., Samaniego, L., Verhoest, N. E. C., van Emmerik, T., Uijlenhoet, R., Achieng, K., Franz, T. E., and Woods, R. (2017). Scaling, similarity, and the fourth paradigm for hydrology. *Hydrology and Earth System Sciences*, 21(7):3701–3713.

Pigram, C. J. and Symonds, P. A. (1991). A review of the timing of the major tectonic events in the New Guinea Orogen. *Journal of Southeast Asian Earth Sciences*, 6(3):307–318.

Ramage, C. S. (1968). Role of a tropical “maritime continent” in the atmospheric circulation. *Monthly Weather Review*, 96(6):365 – 370.

Salinas, D., Flunkert, V., Gasthaus, J., and Januschowski, T. (2020). Deepar: Probabilistic forecasting with autoregressive recurrent networks. *International Journal of Forecasting*, 36(3):1181–1191.

Shen, S. S. P. and Somerville, R. C. J. (2019). *Climate Mathematics: Theory and Applications*. Cambridge University Press.

Smiley, D. (2012). *PyNeurGen: Python Neural Genetic Algorithm Hybrids*. Python library version 0.3.1.

Torrence, C. and Compo, G. P. (1998). A practical guide to wavelet analysis. *Bulletin of the American Meteorological Society*, 79(1):61 – 78.

Wessel, P., Luis, J. F., Uieda, L., Scharroo, R., Wobbe, F., Smith, W. H. F., and Tian, D. (2019). The Generic Mapping Tools Version 6. *Geochemistry, Geophysics, Geosystems*, 20(11):5556–5564.

Wolter, K. and Timlin, M. S. (2011). El niño/southern oscillation behaviour since 1871 as diagnosed in an extended multivariate enso index (mei.ext). *International Journal of Climatology*, 31(7):1074–1087.

Yamanaka, M. D. (2016). Physical climatology of Indonesian maritime continent: An outline to comprehend observational studies. *Atmospheric Research*, 178-179:231–259.

Yang, S., Zhang, T., Li, Z., and Dong, S. (2019). Climate variability over the Maritime Continent and its role in global climate variation: A review. *Journal of Meteorological Research*, 33(6):993–1015.

Yoden, S., Otsuka, S., Trilaksono, N. J., and Hadi, T. W. (2017). *Recent Progress in Research on the Maritime Continent Monsoon*, chapter Chapter 6, pages 63–77.